

The Chromospheric Solar Limb Brightening at Radio, Millimeter, Sub-millimeter, and Infrared Wavelengths

V. De la Luz

CONACYT - SCiESMEX, Instituto de Geofísica, Unidad Michoacán, Universidad Nacional Autónoma de México, Morelia, Michoacán, México. 58190.

Received _____; accepted _____

ABSTRACT

Observations of the emission at radio, millimeter, sub-millimeter, and infrared wavelengths in the center of the solar disk validate the auto-consistence of semi-empirical models of the chromosphere. Theoretically, these models must reproduce the emission at the solar limb. In this work, we tested both the VALC and the C7 semi-empirical models by computing their emission spectrum in the frequency range from 2 GHz to 10 THz, at solar limb altitudes. We calculate the Sun’s theoretical radii as well as their limb brightening. Non-Local Thermodynamic Equilibrium (NLTE) was computed for hydrogen, electron density, and H-. In order to solve the radiative transfer equation a 3D geometry was employed to determine the ray paths and Bremsstrahlung, H-, and inverse Bremsstrahlung opacity sources were integrated in the optical depth. We compared the computed solar radii with high resolution observations at the limb obtained by Clark (1994). We found that there are differences between observed and computed solar radii of 12000 km at 20 GHz, 5000 km at 100 GHz, and 1000 km at 3 THz for both semi-empirical models. A difference of 8000 km in the solar radii was found comparing our results against heights obtained from H α observations of spicules-off at the solar limb. We conclude that the solar radii can not be reproduced by VALC and C7 semi-empirical models at radio - infrared wavelengths. Therefore, the structures in the high chromosphere provides a better measurement of the solar radii and their limb brightening as shown in previous investigations.

Subject headings: Sun: chromosphere — Sun: radio radiation — Sun: infrared —
methods: numerical — radiative transfer — stars: chromospheres

1. Introduction

Following the classical theory of stellar atmospheres, the outer layers of the solar atmosphere must present a single gradient of temperature (Clayton 1983) from the photosphere to the interplanetarium medium. However, observations of the quiet Sun from EUV to Radio in the center of the solar disk (Pawsey & Yabsley 1949; van de Hulst 1953; Zirin et al. 1991; Patsourakos et al. 2007; Vourlidis et al. 2010) show that in order to reproduce the spectra, it is necessary a complex atmosphere structure. Even more, observations by Solanki et al. (1994) confirms the existence of a cool region in the chromosphere, where the CO molecula limit the temperature up to 4000 K. Therefore, the CO molecula fix a lower temperature threshold in the chromospheric models and is called “the Temperature Minimum of the Sun”.

The chromospheric models include hydrostatic (van de Hulst 1953; Allen 1963; Kuznetsova 1978; Ahmad & Kundu 1981; Vernazza et al. 1981; Landi & Chiuderi Drago 2003; Loukitcheva et al. 2004; Chiuderi & Chiuderi Drago 2004; Fontenla et al. 2008), hydrodynamic (HD, Carlsson & Stein 1995, 1997, 2002), and magnetohydrodynamic (MHD) approximations (Loukitcheva et al. 2015). However, the dynamics of the dominant force that allow the existence of CO emission remains as an open question (Penn 2014).

Despite the simplifications of the hydrostatic atmospheres, the semi-empirical models still useful to compute the flux from solar-like atmospheres (Liseau et al. 2015) and flares events (Trottet et al. 2015) at radio - infrared wavelengths.

The semi-empirical models with hydrostatic aproximation are focused in reproduce the emission in the center of the solar disk. Theoretically, these models must reproduce the emission at the solar limb but analysis in these regions are not included in the atmosphere computations. One of the most important characteristic in these upper region of the solar atmosphere is that unlike the limb darkening at visible wavelengths (Kopal 1946), there is

a limb brightening at radio frequencies (McCready et al. 1947) contributing to an increase in the apparent solar radius (Smerd 1950).

Earlier observations between 5 GHz (6 cm) and 33 GHz (9 mm) show clearly a limb brightening (Kundu et al. 1979). Observations at shorter wavelengths (33 GHz and 86 GHz) reported both limb darkening and sharp cutoff distribution (non-limb darkening, Lantos & Kundu 1972; Ade et al. 1974). However, observations with the James Clerk Maxwell radio telescope clearly show solar limb brightening at 850 GHz, 353 GHz, and 250 GHz (350, 850, and 1200 μm respectively, Lindsey et al. 1995).

First attempts to found the sources of these higher emissions between 0.01 GHz (30 m) and 30 GHz (1 cm) at the solar limb showed that the main contributors are the chromosphere and the corona (Martyn 1946; Kopal 1946; Sander 1947; Giovanelli 1948). The role of the fine-structure involved in the quiet Sun emission (spicules) and its relation with the limb brightening at millimeter wavelengths was discussed in the firsts semi-empirical models (Fuerst et al. 1979; Ahmad & Kundu 1981). Further investigations made by Selhorst et al. (2005) showed that the spicules could modulate the morphology of the limb brightening profile. However, the chromospheric empirical model used by Selhorst et al. (2005) is not necessarily a good approximation for the physical conditions in the **low** chromosphere (Carlsson & Stein 2002; De la Luz et al. 2011) when considering a full ionized chromosphere. Observations of the solar limb at $\text{H}\alpha$ (Skogsrud et al. 2014) clearly show spicules in the high chromosphere. Furthermore, Wang et al. (1995) found evidence of solar limb occultation in the radio emission from eruptive events located around the limb.

In this work, we applied the numerical code PakalMPI (De la Luz et al. 2011) to solve the radiative transfer equation (De la Luz et al. 2010) to compute the theoretical spectrum from 2 GHz to 10 THz at limb altitudes using as input VALC (Vernazza et al. 1981) and

C7 (Avrett & Loeser 2008) semi-empirical models. The computed synthetic spectrums are compared against observations by Clark (1994) to test the autoconsistence of VALC and C07 models at the limb. We applied the 3D geometry of PakalMPI to calculate the local emission and absorption processes at several altitudes above the solar limb using the following: i) three opacity sources: Bremsstrahlung, H^- , and inverse Bremsstrahlung, ii) deriving the maximum relative limb brightening from the chromospheric contribution detailing the local emission and absorption process, iii) a numerical approximation to estimate the solar radii for the frequencies observed, and iv) an estimate of the changes in the solar radii

In Section 2, we introduce the chromospheric model. In Section 3, we show the opacity sources and the theoretical computations for the simulated spectra. In Section 4, the results of the comparison of our synthetic spectra for VALC and C7 models versus the observations at millimeter - infrared wavelengths in the solar limb are given. In Section 5, we present our conclusions.

2. The Chromospheric Model

In a previous paper (De la Luz et al. 2011), we introduced the Non-Local Thermodynamic Equilibrium (NLTE) computation of the simulated spectra using an interpolation of the pre-computed departure coefficient b_1 (Menzel 1937) for hydrogen. The b_1 parameter is defined as

$$b_1 = \frac{n_1/n_1^*}{n_k/n_k^*},$$

where n_1^* and n_k^* are the densities of hydrogen in the ground state $n = 1$ and ionized hydrogen in thermodynamic equilibrium (LTE), respectively. The n_1 and n_k represents the same but in NLTE. The b_1 parameter shows if the system is in LTE ($b_1 = 1$) or NLTE ($b_1 \neq 1$). With this technique, we improved the computation time and reduced the

complexity of the numerical solution. We applied b1 parameters published in Vernazza et al. (1981). The input models are: the VALC from Vernazza et al. (1981) and the C7 from Avrett & Loeser (2008). We used these models to compare if the inclusion of the ambipolar diffusion in the C7 chromospheric model is different, if at all, with the classic VALC model in the emission at the limb.

We assumed a static corona as boundary condition for the numerical model. The inclusion of the corona does not modify the final brightness temperature ($T_b(\nu)$) in the frequencies (ν) under study.

In the VALC model (black lines in Figure 1), we used observations from David et al. (1998) of the upper limit in the quiet corona, 2.2×10^5 km above the photosphere and $T = 3.9 \times 10^6$ K. We used Baumbach-Allen formula for the density at high altitudes (Figure 2). The C7 model terminates at 10^5 km. Therefore, we added (as lower boundary for the algorithm) at 1 AU representative values of density and temperature for quiet Sun ($T = 10^5$ K and $H = 10 \text{ cm}^{-3}$). The source of the emission at the frequencies under study comes from the chromosphere region (see Section 4).

Our model includes three opacity sources: Classic Bremsstrahlung (Kurucz 1979), Neutral Interaction (Zheleznyakov 1996; John 1988) and Inverse Bremsstrahlung (Golovinskii & Zon 1980). A study of the contribution in the emission for each opacity source in the center of the solar disk can be found in De la Luz et al. (2011).

3. Computations

PakalMPI (De la Luz et al. 2010) solves the radiative transfer equation for a set of 3D ray paths (or lines of sight from the Earth to the Sun, Figure 3). We intersect two geometric systems: i) the spherical heliocentric and ii) the vanishing point from the Earth to the Sun.

The intersection of both geometry systems define the spatial points where the radiative transfer equation is solved iteratively in a further step. Each ray path provides the solution for a single pixel in a 2D image. The resolution of the image is fixed by the number of lines of sight in the ray path set. As the radial atmospheric stratification (density, temperature, etc) is interpolated onto the ray path, then we used the physical conditions from the 1D radial chromospheric models directly. The center of the Sun is the geometrical point. We control the integration steps (dz) on the z -axis. The origin of the z -axis is the center of the Sun and increments towards the Earth direction. The y -axis is perpendicular to z -axis and represents the radial distance in the solar disk. We defined

$$r = y - R_{sun}$$

as the altitude above the limb, where R_{sun} is the optical solar radii (6.96×10^5 km).

A line of sight is obtained from the 2D image using three elements: the pixel resolution, the spatial resolution, and the distance between the source and the image. We computed a synthetic spectrum from radio to infrared wavelengths for each pixel in our image.

Additionally, PakalMPI take 6 parameters to configure the numerical integration: i) the begin (z_begin), ii) the end (z_end) of the ray path integration over the z -axis, iii) the image resolution in pixels ($-r$), iv) the spatial resolution or zoom ($-Rt$), v) the integration step in km (dz), and vi) the minimal parameter to be considered for this algorithm ($-min$). In this paper, we used the following configuration for PakalMPI:

```
z begin (-z_begin) = -6.96e5 km
z end (-z_end) = 6.96e5 km
Image Resolution (-r) = 9733x9733 px
Spatial Resolution (-Rt) =7.3e5 km
dz (-dz) = 1 km
```

Minimal Parameter (-min) = 1e-40 [I]

In Table 1 we defined the frequency and spatial configuration of the simulated spectra. The first column show range in pixels on the y -axis, where the pixel 0 is the center of the solar disk. The second column define the range in km and the third column the step in km between each point. The fourth column is the range of frequencies for each spatial point and the last column the step in frequency.

4. Results

Figure 4 show the limb brightening for the VALC model and in Figure 5 for the C7 model. We observed three frequency regions in both plots: i) between 2 GHz and 70 GHz where the T_b remains almost constant with height (vertical lines with the same color), ii) a plateau at 2200 km (VALC) and 2100 km (C7) above the limb and between 70 GHz and 1000 GHz where T_b changes abruptly with height (vertical lines change color at these altitudes), and iii) a gradual decrease in T_b for frequencies greater than 1000 GHz (vertical color changes slowly). Between 5 GHz and 100 GHz, the VALC model shows higher limb brightness temperatures than the C7 model.

The maximum relative limb brightening is computed by taking $T_b(\nu)$ at each position and frequency and normalizing it by the brightness temperature in the center of the solar disk $T_{b0}(\nu)$ (Figure 6). A detailed study of this spectrum in the center of the solar disk can be found in De la Luz et al. (2013).

Figures 7 and 8 shows the relative limb brightening ($T_b(\nu)/T_{b0}(\nu)$) for VALC and C7 models respectively. C7 show higher relative brightness temperatures in a higher region than VALC model. In the case of VALC results, we found an unexpected strong relative limb brightening between 15 and 150 GHz as shown in Figure 7 (between the vertical white

lines) which is not observed in the absolute limb brightening. We also found that at around 40 GHz the extension of this unexpected limb brightening is a maximum.

Exploring this relative maximum in the limb brightening, we compared the two semi-empirical models at 15 GHz and 40 GHz. In Figure 9 we plot $T_b(\nu)$ vs height above the limb at 15 GHz and 40 GHz for the two models. We found that for the C7 model the limb brightening at 15 GHz is higher than 40 GHz. However, we found the opposite in the relative limb brightening ($T_b(\nu)/T_{b0}(\nu)$) for the VALC model (Figure 10).

We analyzed the pixel indicating 900 km above the limb at 15 and 40 GHz (white points in the Figure 7). For the VALC model we found a strong decrease at 15 GHz, and a strong increase at 40 GHz in the shape of the relative limb brightening.

Figure 11 and 12 shows the convergence of T_b and T_b/T_{b0} on the z -axis for VALC and C7 models taking into account two frequencies: 15 and 40 GHz. These figures shows the local contribution to the final T_b and T_b/T_{b0} . For both cases, the main contribution to the emission process takes place around 42×10^3 and 46×10^3 km on the z -axis. Note for the VALC at 15 GHz a plateau is formed between 43×10^3 and 45×10^3 Km. This structure is not observed at 40 GHz.

Figure 13 show the optical depth for Bremsstrahlung and H^- on the z -axis for the pixel indicating 900 km above the limb. VALC model found a region (on the z -axis) at 43×10^3 where the opacity decreases slowly until 46×10^3 km (compared with C7 model).

Figure 14 show that for 43×10^3 km and 46×10^3 km on z -axis corresponds the distance above the photosphere (r) of 2.1×10^3 km and 2.3×10^3 km respectively, i.e. we found that the plateau in the radiative transfer process is originated by the plateau in the radial temperature profile of the VALC model. We applied this principle for each altitude in this study. Figure 15 shows the temperature limits to be evaluated by PakalMPI for a particular

height above the limb, the yellow boxes defines the height above the limb (ray path) and the arrow points the temperature limit on the temperature model.

With figures 7 and 8, we computed the solar radii at frequency ν as the isophote where

$$T_b(\nu)/T_{b0}(\nu) = 0.5.$$

In order to compare the synthetic spectrums, we included high resolution observations of the solar radii with the solar eclipse occultation technique (Clark 1994) carried out by the James Clerk Maxwell Telescope. The computed solar radii from observations using polinomial function degree 2 is:

$$R_{sun}(\nu[GHz])[km] = 3.42 \times 10^4 - 1.81 \times 10^4 \log(\nu) + 2420 \log^2(\nu) \quad (1)$$

The Figure 16 compares the computed theoretical solar radii versus the high resolution observations. The theoretical radii from both models is close in all the frequency ranges. In Figure 17, we plotted the diferences between the synthetic solar radii and the observed. We found a maximum difference of 12000 km at 20 GHz.

5. Conclusions

We presented the first set of normalized solar synthetic spectrums from 2 GHz to 10 THz between 0 km and 4500 km above the solar limb. We used both semi-empirical models: VALC (Vernazza et al. 1981) and C7 (Avrett & Loeser 2008) as input in the physical conditions of the chromosphere (Figures 1 and 2). The radiative transfer equation was solved by PakalMPI (De la Luz et al. 2010) in a 3D geometry above the limb (Figure 3). NLTE computations were carried out for calculate ionization states, including hydrogen, electron density, and H^- . Bremsstrahlung, H^- , and Inverse Bremsstrahlung (De la Luz et al. 2011) where used in the computation of the optical depth.

The synthetic spectrums computed by PakalMPI in the paths above the limb were taken into account to calculate the theoretical solar limb brightening (Figures 4 and 5). The theoretical spectrum in the center of the solar disk (Figure 6) was used to compute the relative limb brightening T_b/T_{b0} at altitudes above the limb (Figures 7 and 8). The radiative transfer process between 15 and 150 GHz (where we found an unexpected strong relative limb brightening) was analyzed (Figures 9, 10, 11, 12, 13, and 14). Finally, we calculated the theoretical solar radii and compared the results (Figures 16 and 17) with previous observations by Clark (1994).

In both semi-empirical models, we found three regions in frequency where the rise of T_b with respect to the height above the limb changes significantly: 2 GHz - 70 GHz, 70 GHz - 1000 GHz, and 1000 GHz - 10000 GHz. VALC model shows higher limb brightness temperatures than the C7 model between 5 GHz and 100 GHz. The relation between the limb brightening and the radial temperature profile is related with the minimal distance between the ray path (used to compute the radiative transfer equation) and the photosphere (Figure 15). The minimal distance is the lower boundary in the radial temperature profile used to compute the emission.

The normalization in frequency of the spectrum by their emission in the center of the solar disk (Figures 7 and 8) provides a tool to test semi-empirical models of the chromosphere above the limb. We found that the unexpected relative limb brightening in the VALC model between 15 and 150 GHz is caused by the plateau in temperature of the radial temperature profile of the VALC model (Figure 13). The inclusion of ambipolar diffusion (C7 model) reduces the relative limb brightening in this region (Figures 11 and 12).

The solar radii obtained by the relative limb brightening show differences of 12000 km at 20 GHz, 5000 km at 100 GHz, and 1000 km at 3 THz if there are compared against

previous observations (Clark 1994). These differences are observed for both semi-empirical models.

Our results show that the stratified chromospheric models used in this study are not enough to reproduce the solar radii at frequencies lower than 400 GHz, and suggest other structures evolved in the emission process (Figure 16).

In this context, recent observations of emission of spicules-off the solar limb at $H\alpha$ (Skogsrud et al. 2014) show a clear emission of 4000 km above the limb, indicating that the individual spicules structures extend above 4000 km. This kind of spicules are called type II (from quiet Sun regions). The highest altitudes measured of the individual spicules rise 8000 km above the limb. However, observations at 20 GHz (Clark 1994) have shown the existence of structures that rise 20000 km above the limb. There is a maximum difference between the computed theoretical solar radii and observations by Clark (1994) of 12000 km at 20 GHz (see Figure 17) that chromospheric semi-empirical models (Vernazza et al. 1981; Avrett & Loeser 2008) can not reproduce. This $H\alpha$ emission observed from the spicules type II (Skogsrud et al. 2014) suggest that for altitudes lower than 8000 km above the limb, temperature of the region is lower than the ionized temperature for hydrogen. However, this temperature difference is not enough to explain the solar radii at low frequencies. At high frequencies, we found that the difference between simulations and observations decreases to 5000 km at 100 GHz and 1000 km at 3 THz.

If the spicules are the cause of the observed large solar radii at low frequencies, then the spicules should rise to altitudes of about 20000 km above the limb. The millimeter emission at 8000 km above the solar limb can be explained by Bremsstrahlung of full ionized hydrogen which we can not observe in $H\alpha$.

Our results, suggest that the inclusion of the micro-structure in the high chromosphere must be considered when investigating the solar limb brightening and therefore in the models

focused in the center of the solar disk as shown in previous works (Ahmad & Kundu 1981; Roellig et al. 1991; Clark 1994; de Pontieu et al. 2007; Iwai & Shimojo 2015; White et al. 2006; Loukitcheva et al. 2015).

Finally, this study is usefull to undestand the limb occultation by solar microwave sources in eruptive events (Wang et al. 1995) and to characterize planetary transits for solar-like stars at millimeter, sub-millimeter and infrared wavelengths. For the case of planetary transits, the values of radii and their limb brightening are fundamental in the characterization of the light curve (Selhorst et al. 2013) recorded during planet transits at these wavelengths.

This work was supported by the Cátedras CONACyT Fellowship. We are grateful to J. Americo Gonzalez-Esparza and Ernesto Aguilar for their valuable comments.

REFERENCES

- Ade, P. A. R., Rather, J. D. G., & Clegg, P. E. 1974, *ApJ*, 187, 389
- Ahmad, I. A., & Kundu, M. R. 1981, *Sol. Phys.*, 69, 273
- Allen, C. W. 1963, in *IAU Symposium, Vol. 16, The Solar Corona*, ed. J. W. Evans, 1–+
- Avrett, E. H., & Loeser, R. 2008, *ApJS*, 175, 229
- Carlsson, M., & Stein, R. F. 1995, *ApJ*, 440, L29
- . 1997, *ApJ*, 481, 500
- . 2002, *ApJ*, 572, 626
- Chiuderi, C., & Chiuderi Drago, F. 2004, *A&A*, 422, 331
- Clark, T. A. 1994, in *IAU Symposium, Vol. 154, Infrared Solar Physics*, ed. D. M. Rabin, J. T. Jefferies, & C. Lindsey, 139
- Clayton, D. D. 1983, *Principles of stellar evolution and nucleosynthesis*
- David, C., Gabriel, A. H., Bely-Dubau, F., Fludra, A., Lemaire, P., & Wilhelm, K. 1998, *A&A*, 336, L90
- De la Luz, V., Lara, A., Mendoza-Torres, J. E., & Selhorst, C. L. 2010, *ApJS*, 188, 437
- De la Luz, V., Lara, A., & Raulin, J.-P. 2011, *ApJ*, 737, 1
- De la Luz, V., Raulin, J.-P., & Lara, A. 2013, *ApJ*, 762, 84
- de Pontieu, B., McIntosh, S., Hansteen, V. H., Carlsson, M., Schrijver, C. J., Tarbell, T. D., Title, A. M., Shine, R. A., Suematsu, Y., Tsuneta, S., Katsukawa, Y., Ichimoto, K., Shimizu, T., & Nagata, S. 2007, *PASJ*, 59, 655

- Fontenla, J. M., Peterson, W. K., & Harder, J. 2008, *A&A*, 480, 839
- Fuerst, E., Hirth, W., & Lantos, P. 1979, *Sol. Phys.*, 63, 257
- Giovanelli, R. G. 1948, *Nature*, 161, 133
- Golovinskii, P. A., & Zon, B. A. 1980, *Zhurnal Tekhnicheskoi Fiziki*, 50, 1847
- Iwai, K., & Shimojo, M. 2015, *ApJ*, 804, 48
- John, T. L. 1988, *A&A*, 193, 189
- Kopal, Z. 1946, *ApJ*, 104, 60
- Kundu, M. R., Rao, A. P., Erskine, F. T., & Bregman, J. D. 1979, *ApJ*, 234, 1122
- Kurucz, R. L. 1979, *ApJS*, 40, 1
- Kuznetsova, N. A. 1978, *Soviet Astronomy*, 22, 345
- Landi, E., & Chiuderi Drago, F. 2003, *ApJ*, 589, 1054
- Lantos, P., & Kundu, M. R. 1972, *A&A*, 21, 119
- Lindsey, C., Kopp, G., Clark, T. A., & Watt, G. 1995, *ApJ*, 453, 511
- Liseau, R., Vlemmings, W., Bayo, A., Bertone, E., Black, J. H., del Burgo, C., Chavez, M., Danchi, W., De la Luz, V., Eiroa, C., Ertel, S., Fridlund, M. C. W., Justtanont, K., Krivov, A., Marshall, J. P., Mora, A., Montesinos, B., Nyman, L.-A., Olofsson, G., Sanz-Forcada, J., Thébault, P., & White, G. J. 2015, *A&A*, 573, L4
- Loukitcheva, M., Solanki, S. K., Carlsson, M., & Stein, R. F. 2004, *A&A*, 419, 747
- Loukitcheva, M., Solanki, S. K., Carlsson, M., & White, S. M. 2015, *A&A*, 575, A15
- Martyn, D. F. 1946, *Nature*, 158, 632

- McCready, L. L., Pawsey, J. L., & Payne-Scott, R. 1947, Royal Society of London Proceedings Series A, 190, 357
- Menzel, D. H. 1937, ApJ, 85, 330
- Patsourakos, S., Gouttebroze, P., & Vourlidas, A. 2007, ApJ, 664, 1214
- Pawsey, J. L., & Yabsley, D. E. 1949, Australian Journal of Scientific Research A Physical Sciences, 2, 198
- Penn, M. J. 2014, Living Reviews in Solar Physics, 11
- Roellig, T. L., Becklin, E. E., Jefferies, J. T., Kopp, G. A., Lindsey, C. A., Orrall, F. Q., & Werner, M. W. 1991, ApJ, 381, 288
- Sander, K. F. 1947, Nature, 159, 506
- Selhorst, C. L., Barbosa, C. L., & Válio, A. 2013, ApJ, 777, L34
- Selhorst, C. L., Silva, A. V. R., & Costa, J. E. R. 2005, A&A, 440, 367
- Skogsrud, H., Rouppe van der Voort, L., & De Pontieu, B. 2014, ApJ, 795, L23
- Smerd, S. F. 1950, Australian Journal of Scientific Research A Physical Sciences, 3, 34
- Solanki, S. K., Livingston, W., & Ayres, T. 1994, Science, 263, 64
- Trottet, G., Raulin, J.-P., Mackinnon, A., Giménez de Castro, G., Simões, P. J. A., Cabezas, D., de La Luz, V., Luoni, M., & Kaufmann, P. 2015, Sol. Phys., 290, 2809
- van de Hulst, H. C. 1953, The Chromosphere and the Corona (The Sun), 207–+
- Vernazza, J. E., Avrett, E. H., & Loeser, R. 1981, ApJS, 45, 635

- Vourlidas, A., Sanchez Andrade-Nuño, B., Landi, E., Patsourakos, S., Teriaca, L., Schühle, U., Korendyke, C. M., & Nestoras, I. 2010, *Sol. Phys.*, 261, 53
- Wang, H., Gary, D. E., Zirin, H., Kosugi, T., Schwartz, R. A., & Linford, G. 1995, *ApJ*, 444, L115
- White, S. M., Loukitcheva, M., & Solanki, S. K. 2006, *A&A*, 456, 697
- Zheleznyakov, V. V., ed. 1996, *Astrophysics and Space Science Library*, Vol. 204, *Radiation in Astrophysical Plasmas*
- Zirin, H., Baumert, B. M., & Hurford, G. J. 1991, *ApJ*, 370, 779

Table 1: Spacial configuration of the simulations. The first column defines range in pixels on the y -axis (where the pixel 0 is the center of the solar disk), the second column the range in km, the third column the step in km between each point. The fourth column is the range of frequencies for each spatial point and the last column the step in frequency.

y -axis		Frequencies [GHz]		
Range [px]	Range [Km]	Step [km]	Range	Step
			[2,10]	0.5
[4638,4669]	[695700,700350]	150	[10,100]	5
			[100,1000]	50
			[1000,10000]	500
[4680,4780]	[702000,717000]	1500	[2,11]	1

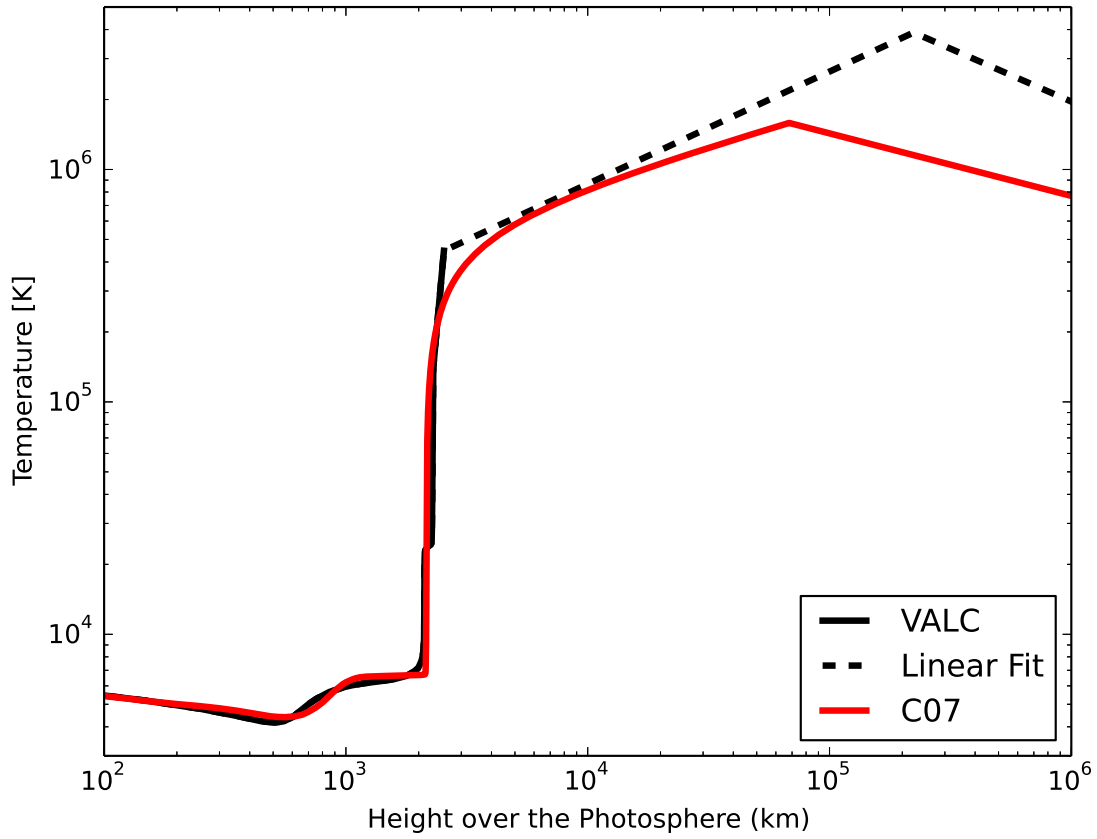


Fig. 1.— Radial temperature profile for VALC (continuous black) and C7 (continuous red). The dashed line is the linear interpolation to fit corona altitudes for VALC model. The C7 model includes the ambipolar diffusion that generates a profile without plateau at 20000 km above the photosphere.

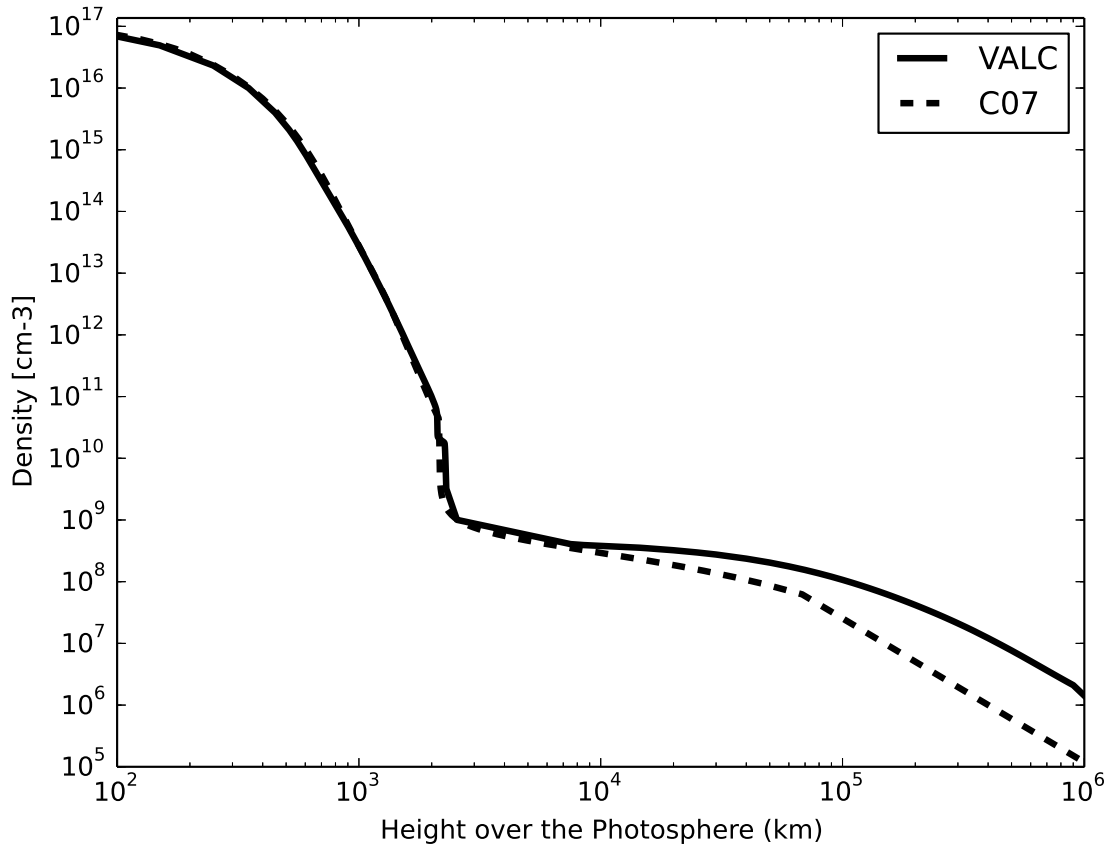


Fig. 2.— Density models for the corona. In black VALC + Baumbach-Allen formula and dashed line for C7 model.

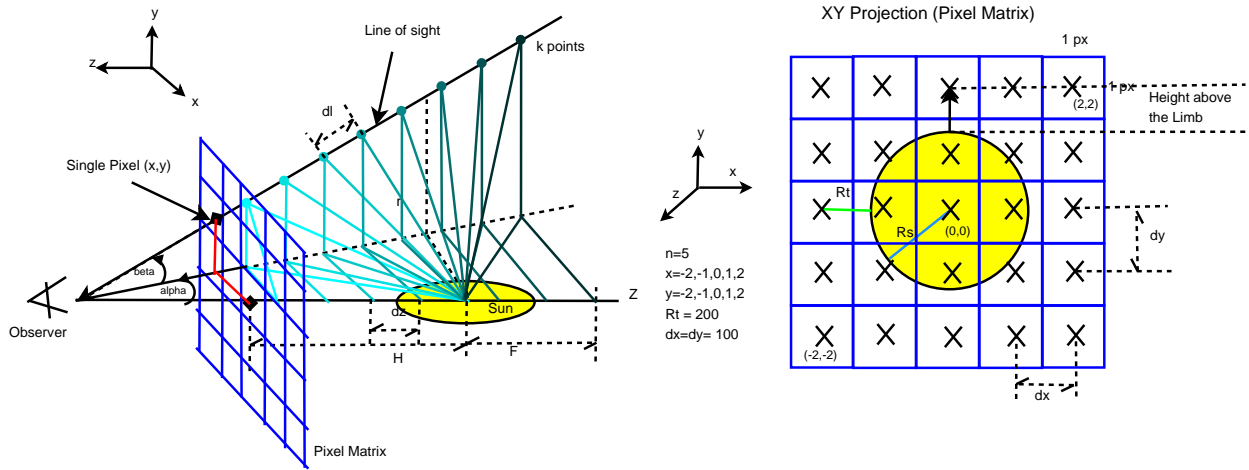


Fig. 3.— Left panel: 3D geometry used to solve the radiative transfer equation. Each line of sight (or ray path) defines the pixel matrix. We can solve this geometry using 2 parameters: the size of the image in km (R_t) and the resolution in pixels of the Pixel Matrix (n). Right panel: Example of Pixel Matrix using $n = 5$ and $R_t = 200$ km. In this figure we define the height above the limb as the distance between the border of solar disk projected in the Pixel Matrix and a point in the Matrix.

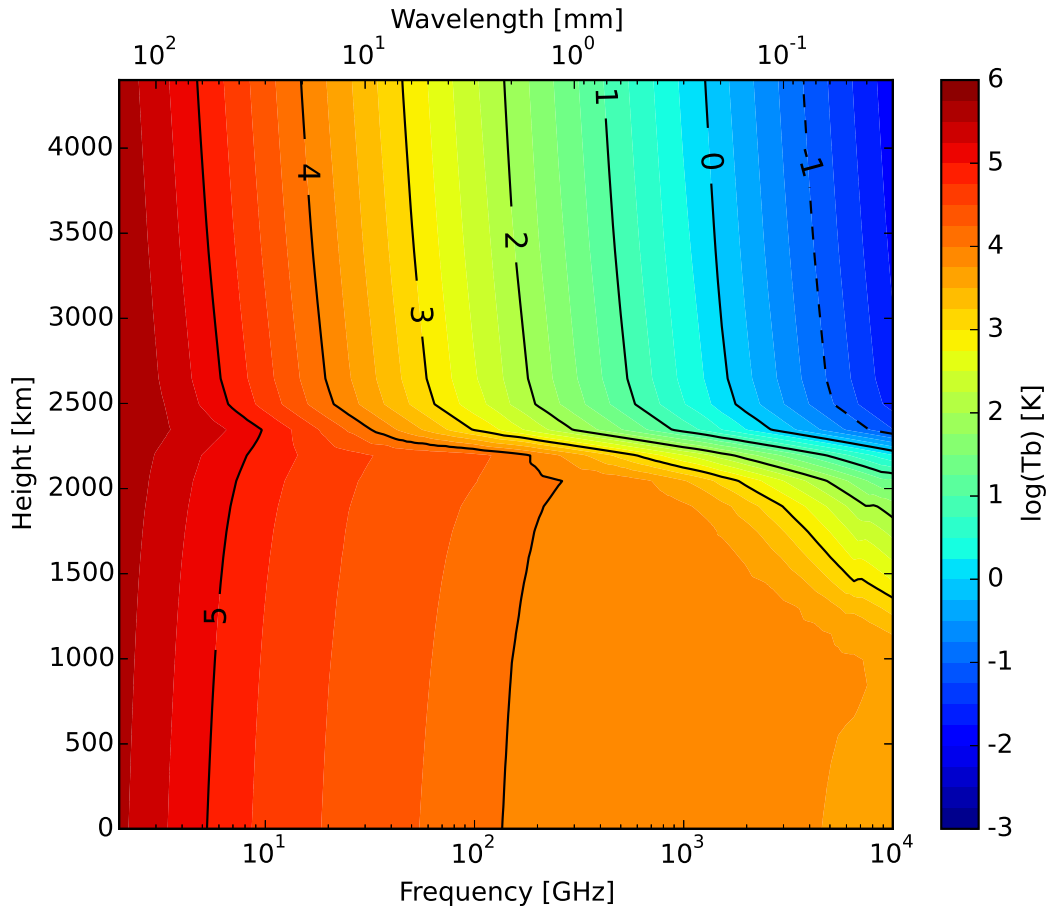


Fig. 4.— Limb brightening using VALC model: x-axis is the frequency in GHz, y-axis is the height above the solar limb (off limb), and in colors we plot the Brightness Temperature ($\log(T_b)$). The figure shows a region at 2200 km above the limb and between 50 and 1000 GHz where T_b strongly decrease.

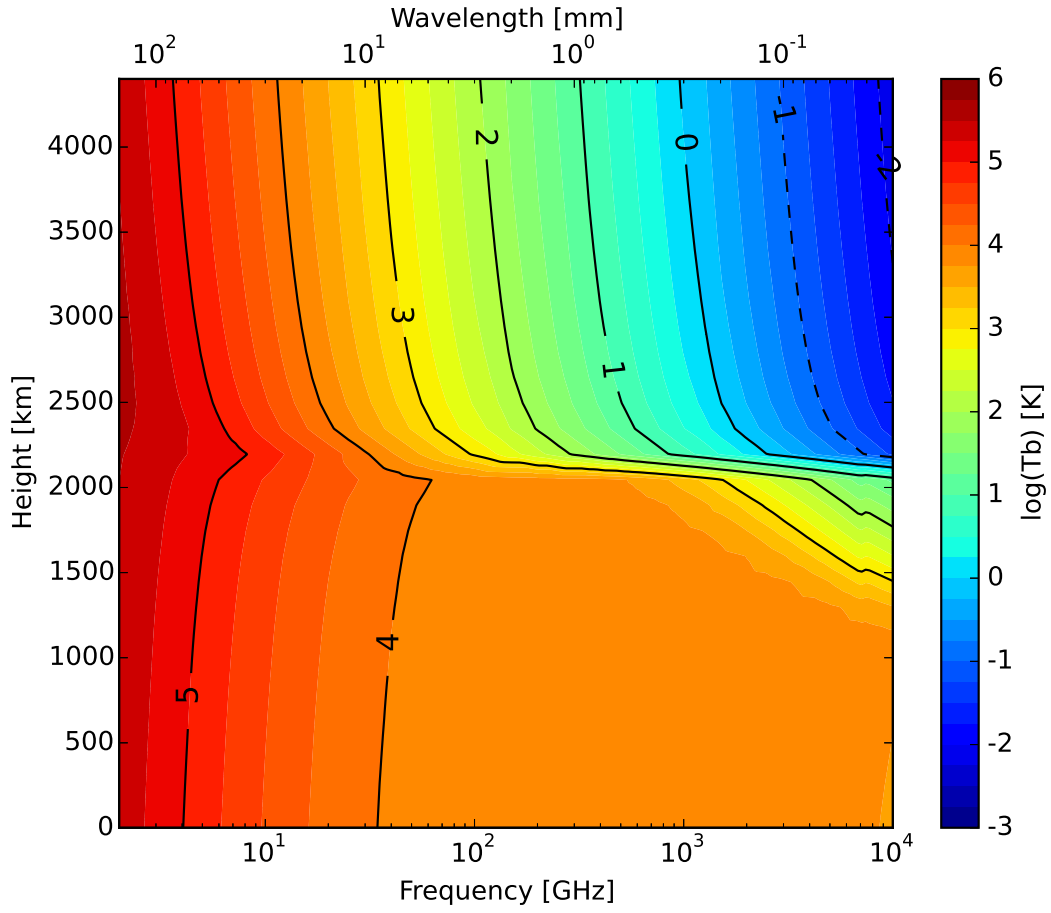


Fig. 5.— Limb brightening using C7 model. This model shows lower T_b compared to VALC model but we also observe the interface in T_b between 50 and 1000 GHz at 2100 km above the limb.

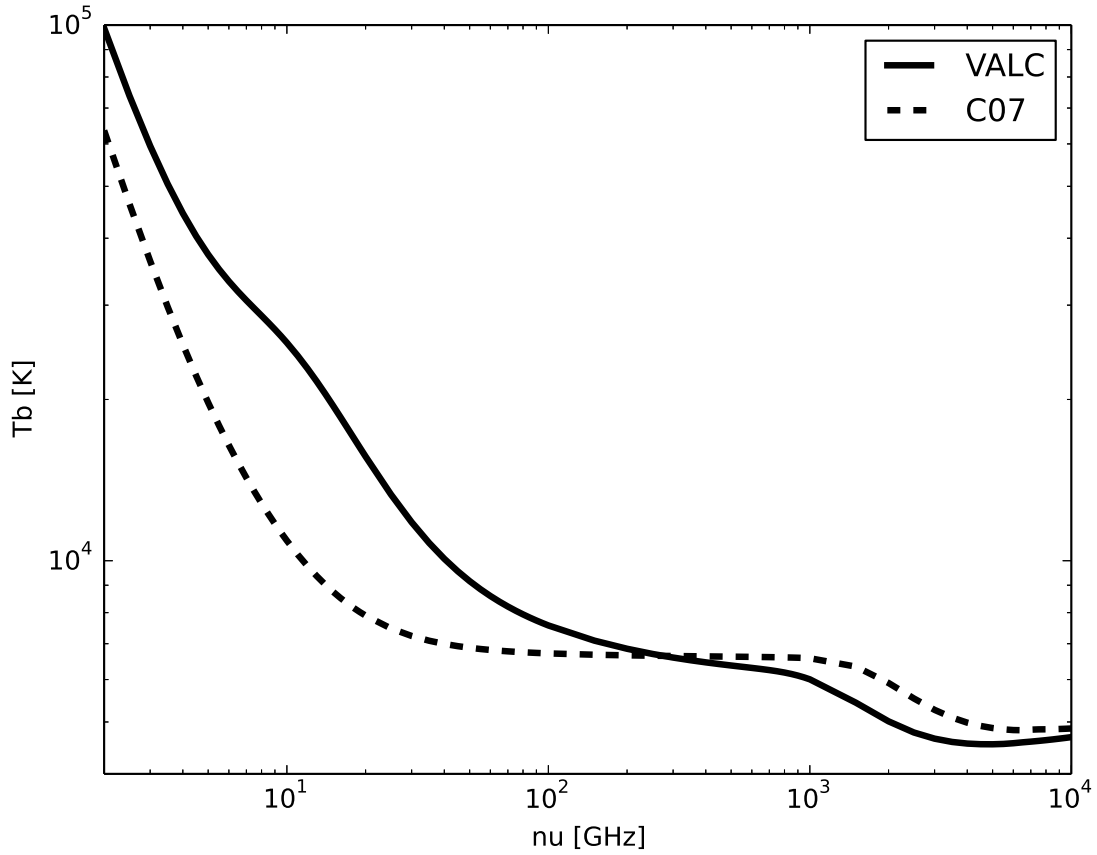


Fig. 6.— Synthetic spectrum in the center of the solar disk for VALC (continuous) and C7 (dashed). VALC shows higher T_b than C7 for frequencies lower than 300 GHz. In frequencies higher than 300 GHz VALC shows lower T_b than C7 model. A detailed study of the spectrum in the center of the solar disk can be found in De la Luz et al. (2011)

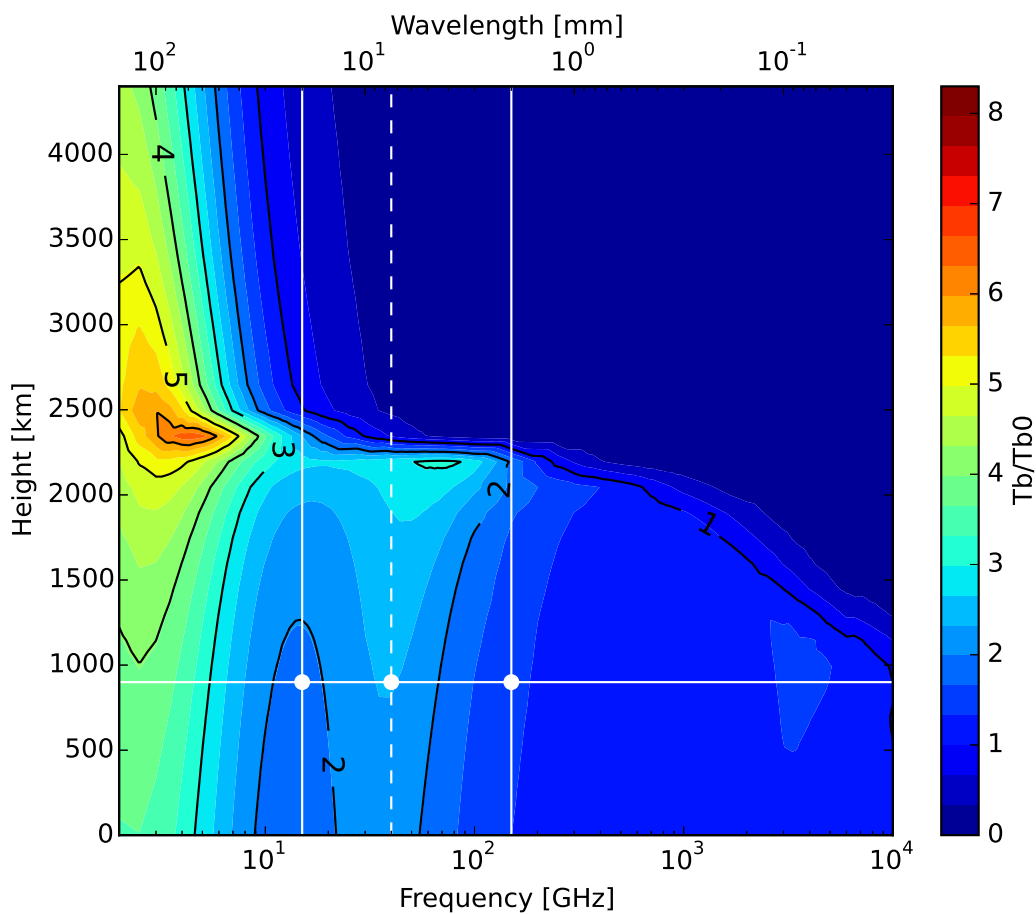


Fig. 7.— Relative limb brightening using VALC model. In colors we plot T_b/T_{b0} for each frequency for each height above the limb using the spatial configuration defined in Table 1. The figure shows an unexpected high relative limb brightening between 15 and 150 GHz. The dashed vertical line shows the frequency where the unexpected relative limb brightening has a maximum extension (40 GHz).

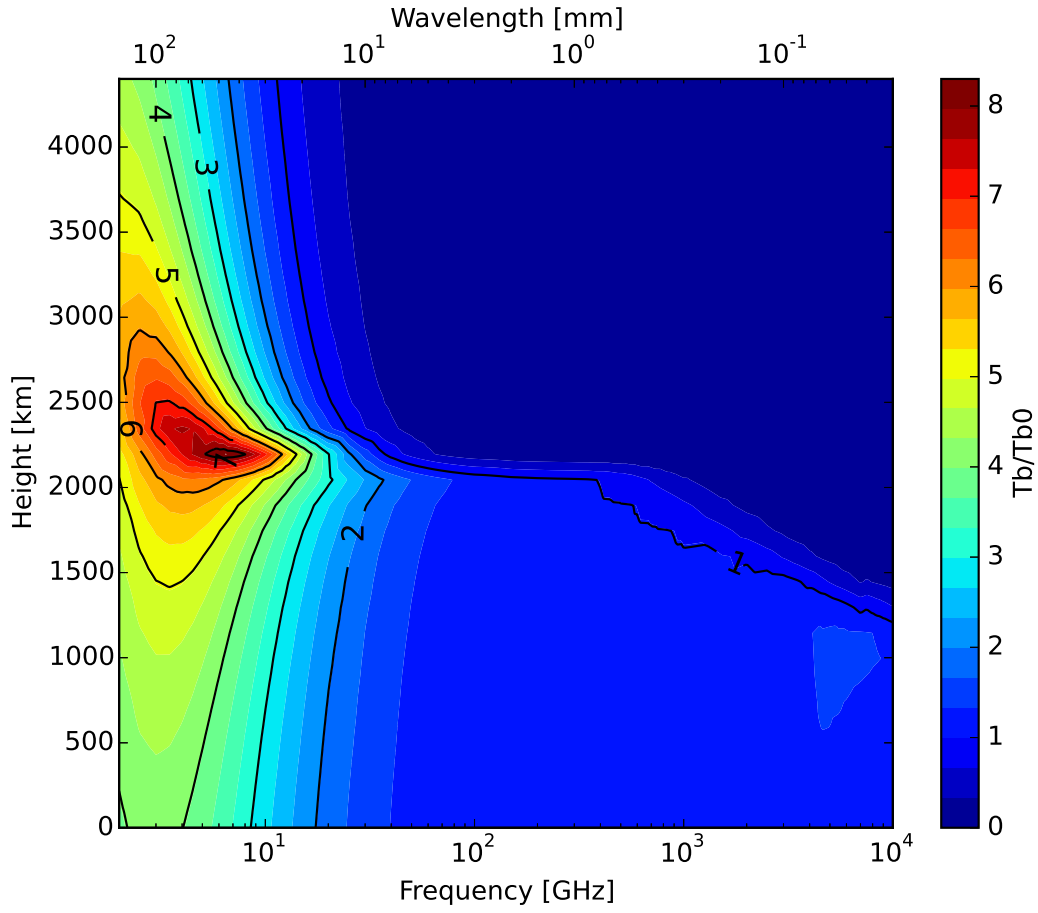


Fig. 8.— Relative limb brightening using C7 model. This model shows higher relative brightness temperatures than VALC model. The peak of maximum relative limb brightening is between 2 and 10 GHz.

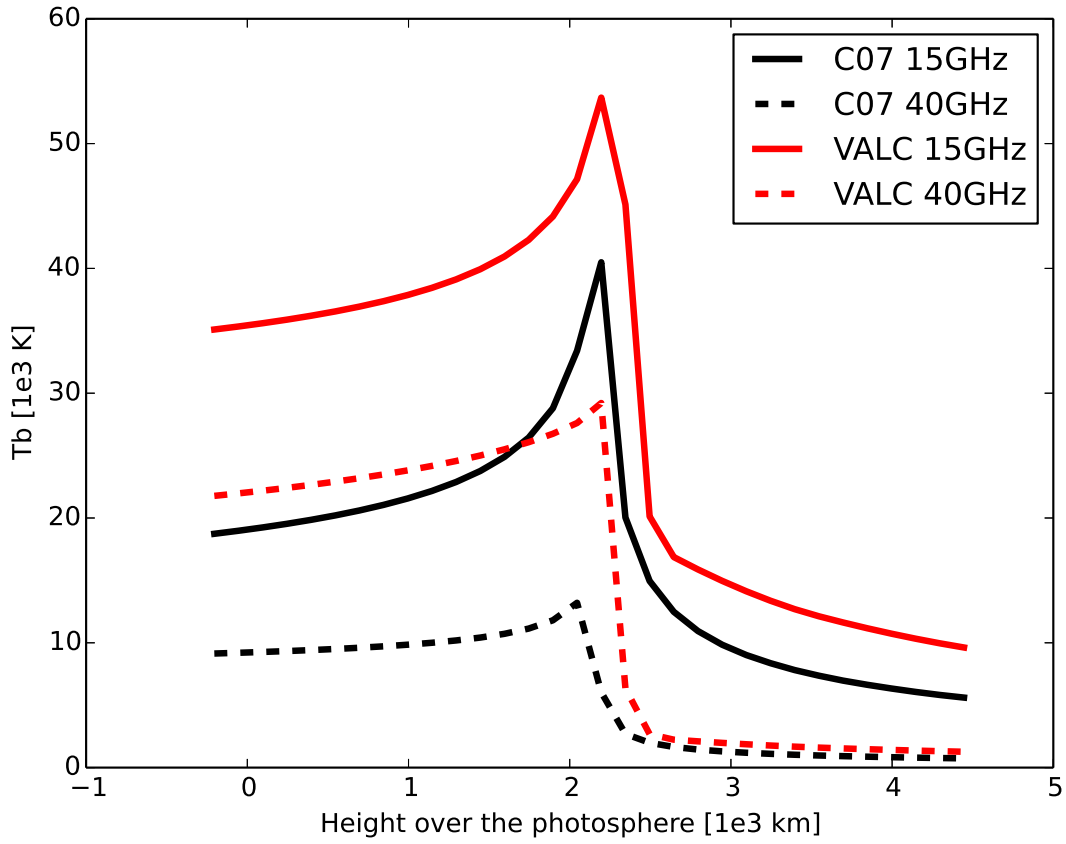


Fig. 9.— Limb brightening for 15 GHz and 40 GHz using C7 and VALC models. C7 shows lower T_b than VALC model. Both models show the classical limb brightening.

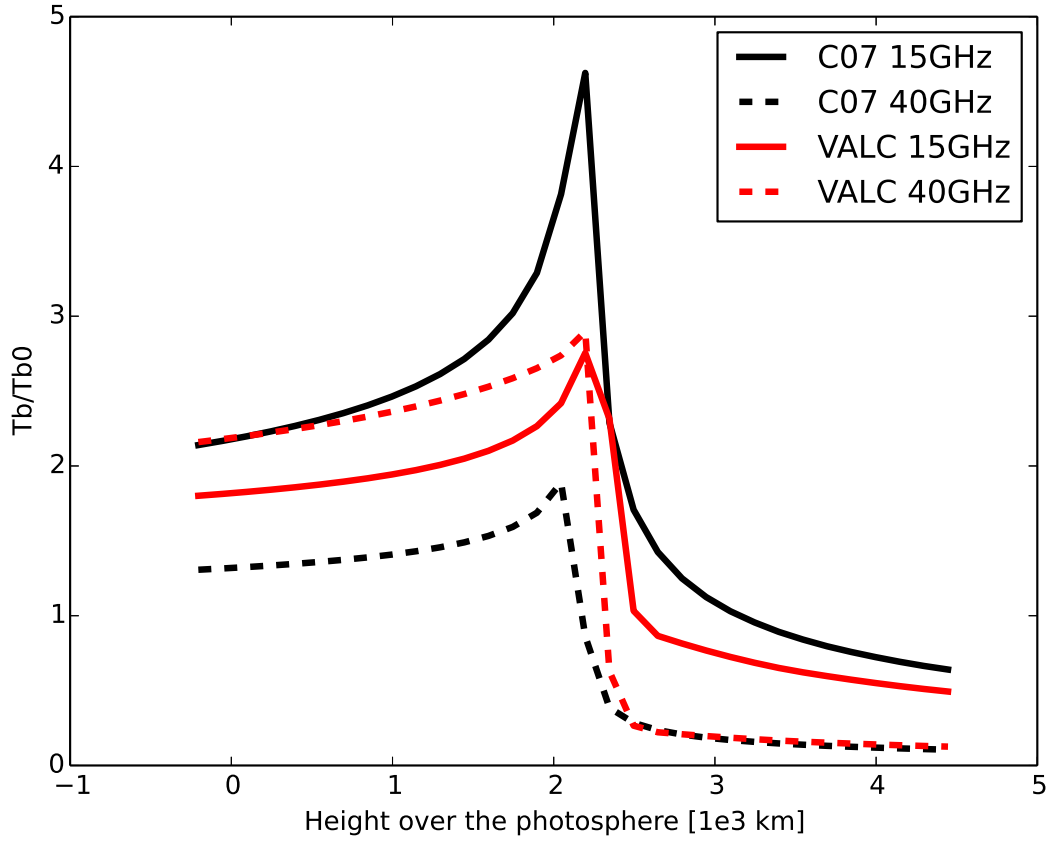


Fig. 10.— Comparison between relative limb brightening for 15 and 40 GHz using both models at solar limb altitudes. C7 shows the expected result (higher frequency has lower T_b) like classical limb brightening. VALC shows the opposite. The maximum limb brightening at 15 GHz and 40 GHz has the same T_b .

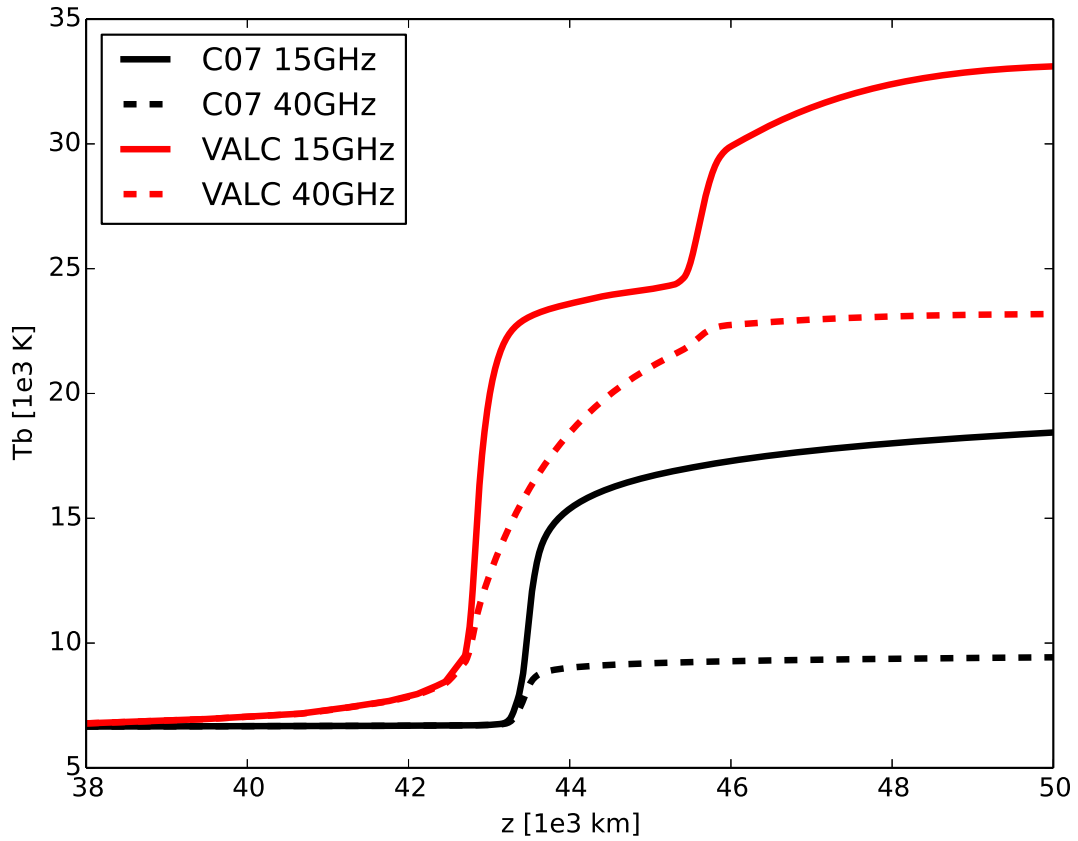


Fig. 11.— T_b for 15 GHz and 40 GHz for VALC and C7 models in the ray path projected onto the z axis at a height above the limb of 900 km. The profile for VALC at 15 GHz presents two major increases in the emission at 42500 and 45500 km in z .

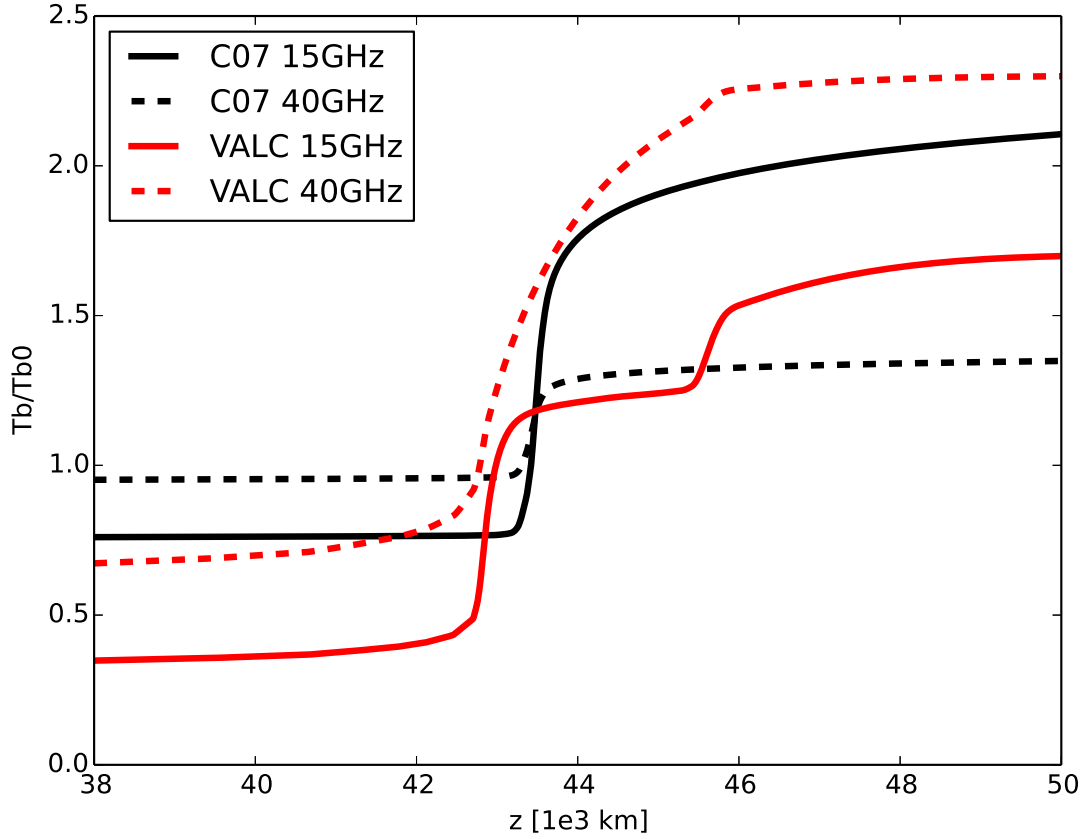


Fig. 12.— When dividing T_b by T_{b0} , the large difference in T_{b0} computed by VALC model at 15 GHz and 40 GHz results in a high relative brightness temperature at 40 GHz than 15 GHz. We also observe the second increase in relative limb brightening at 45500 km in z that is not shown in the other profiles.

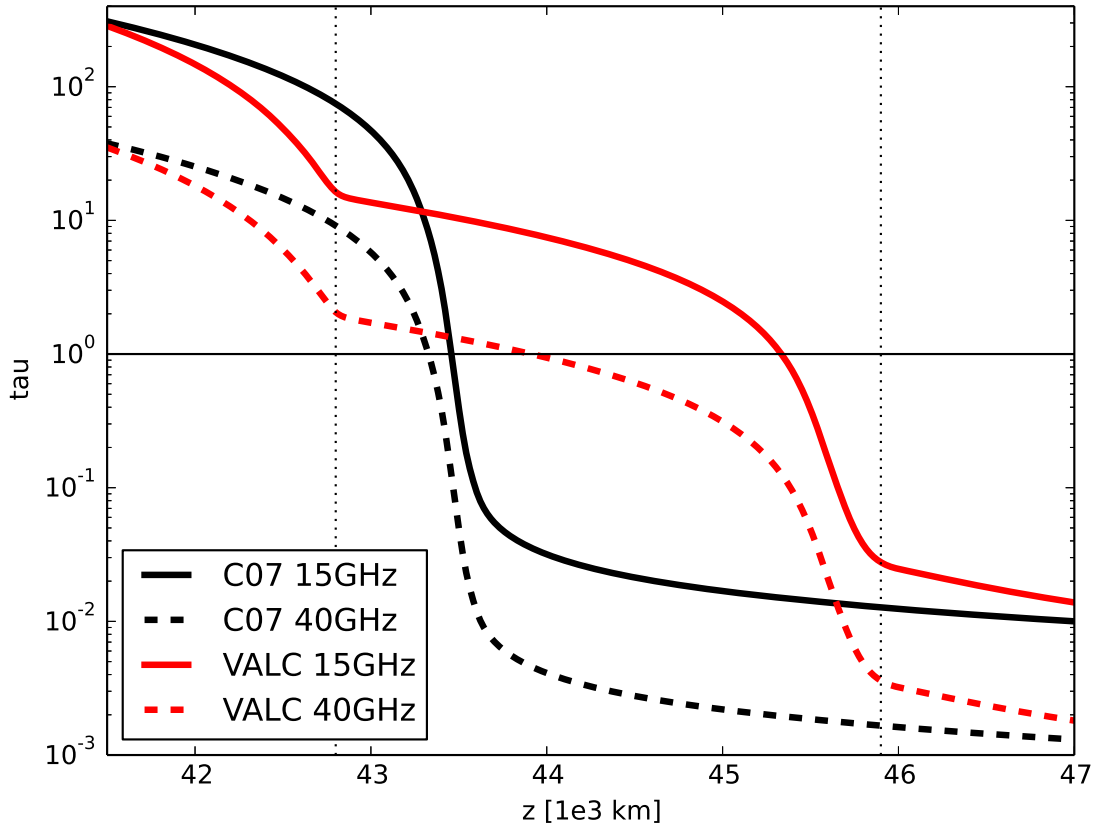


Fig. 13.— Optical depth for C7 (black) and VALC (red) models at 15 GHz (continuous) and 40 GHz (dashed) at altitude above the limb at 900 km. We found that the cause of the second region of emission for VALC at 15 GHz is the plateau in tau close to 1 is between 43000 and 46000 km in z .

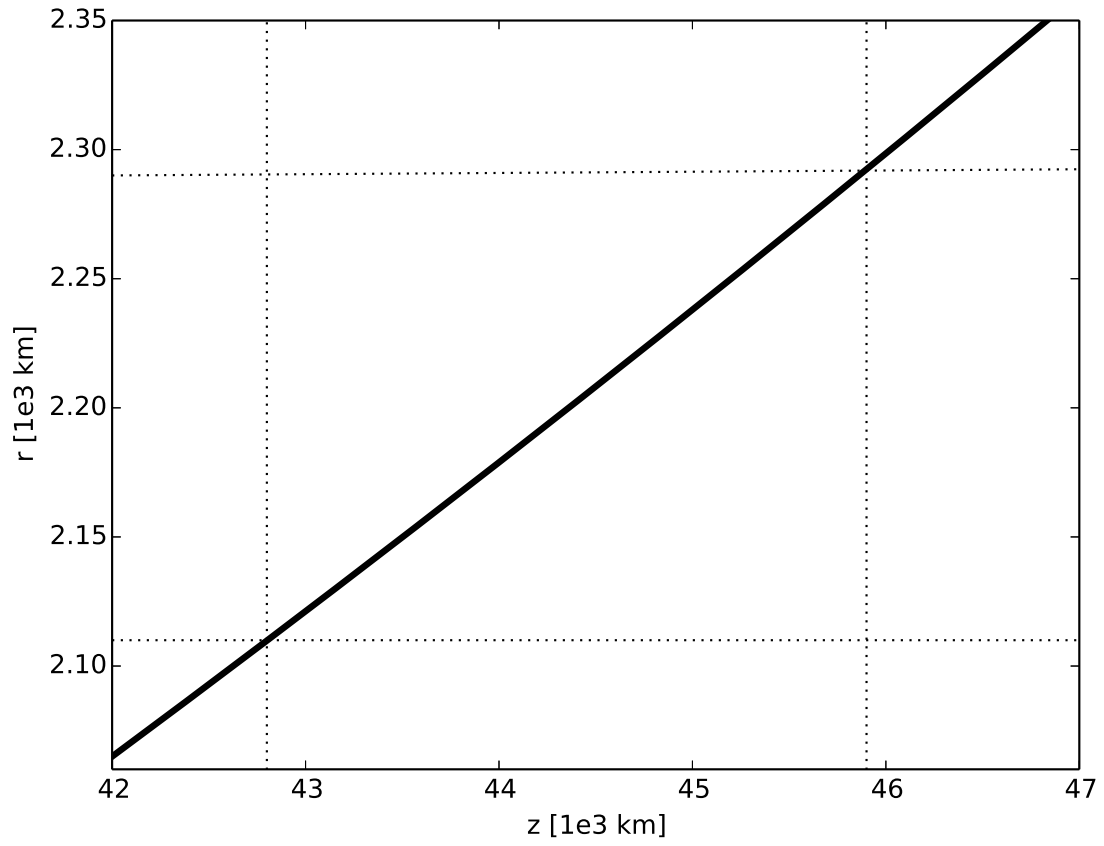


Fig. 14.— Photosphere distance r in function of z for a ray path at 900 km above the limb.

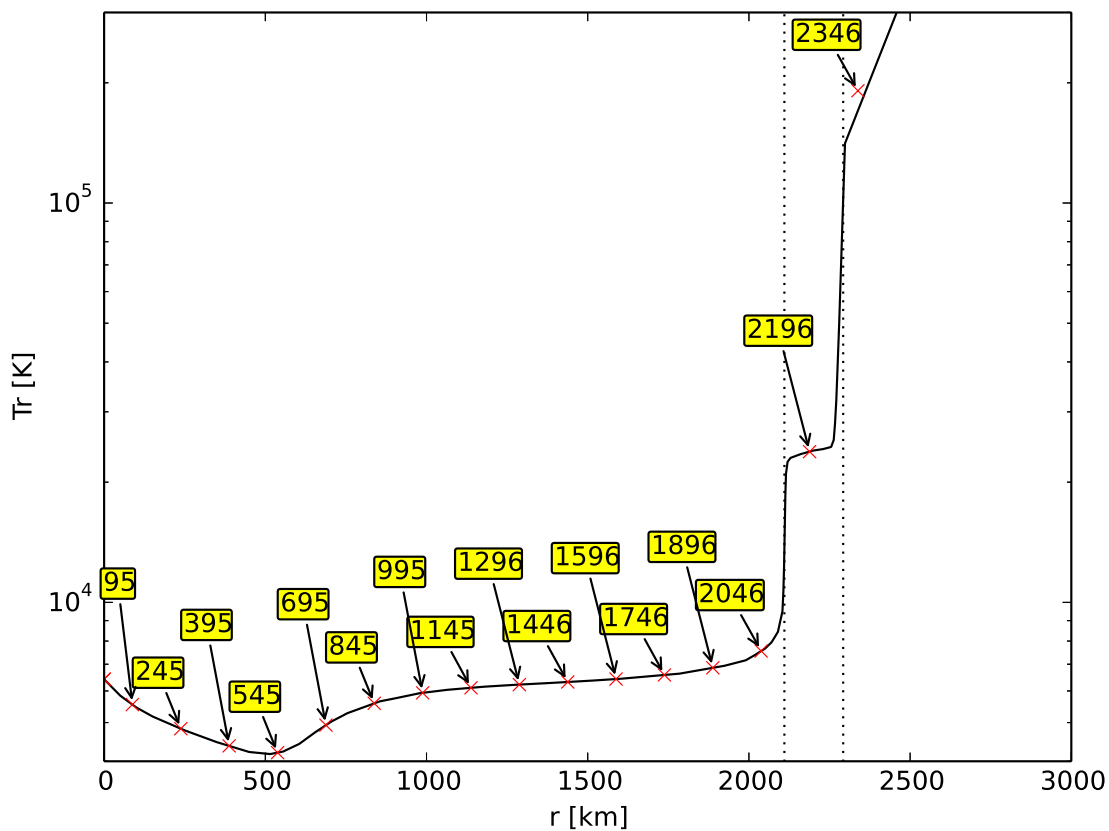


Fig. 15.— We show the radial temperature profile T_r from the VALC model that is used for computing the T_b . In yellow are the heights in km above the limb where the radiative transfer equation is computed. The red cruces show the lower boundary in temperature on the radial profile that is used to solve the RTE for each ray path. For example at 2196 km above the limb the model used temperatures from the radial temperature profile above 2200 km.

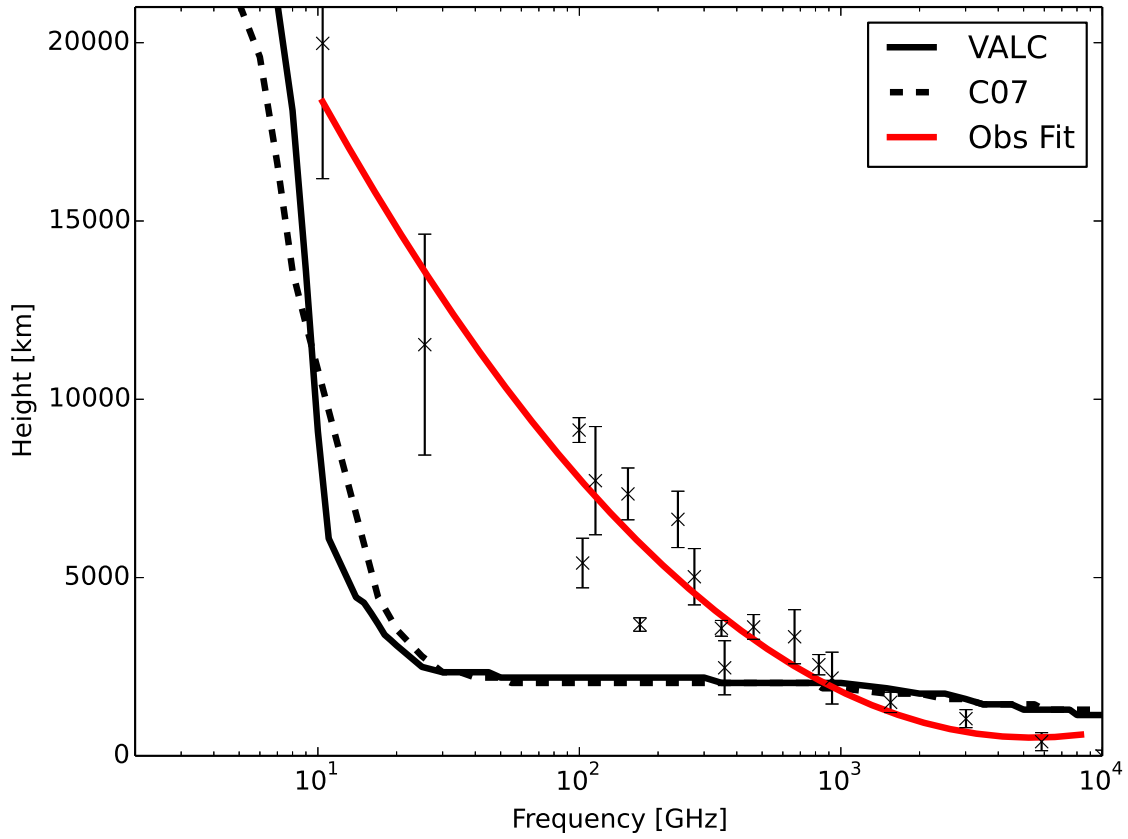


Fig. 16.— Simulated solar radii for VALC (continuous blackline) and C7 (dashed black line) models vs observations. The cross points with error bars are the observations from Clark (1994) and the continuous red line is their polynomial fit. The emission from the chromospheric models can not reproduce the solar radii.

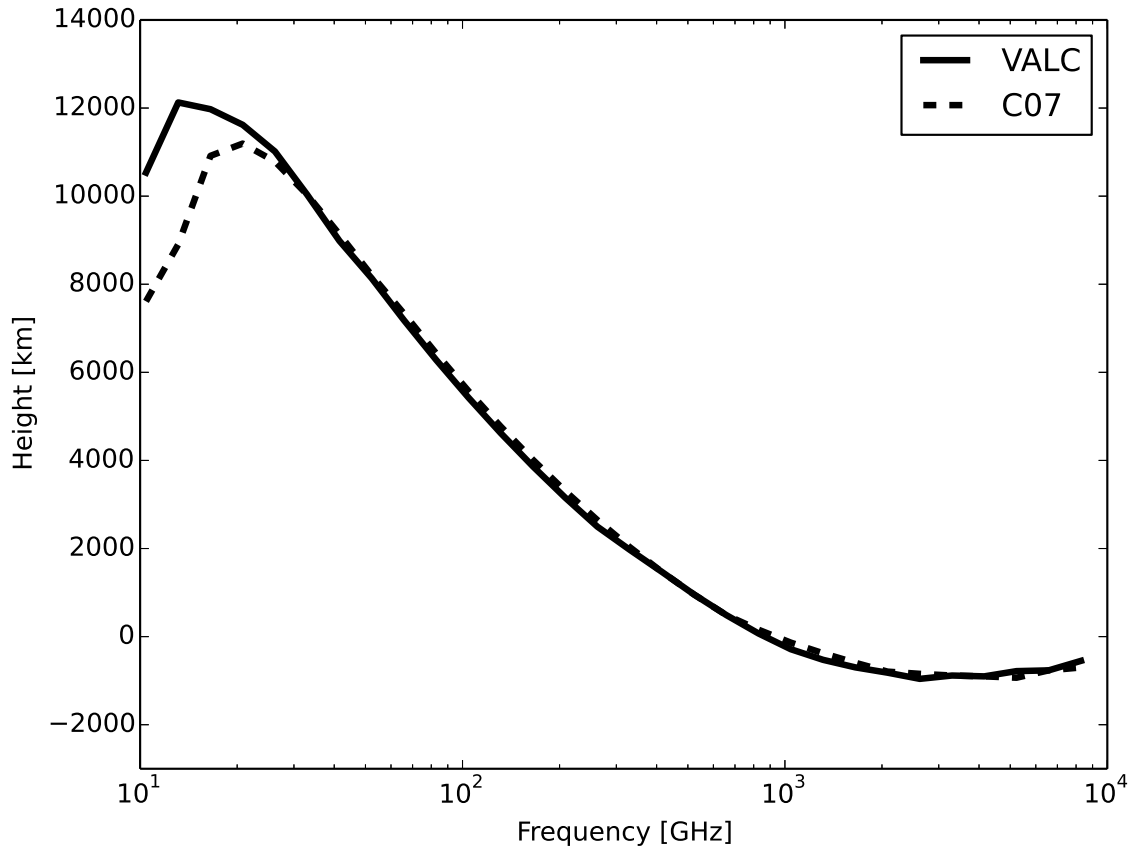


Fig. 17.— Difference between observations from Clark (1994) and this work. The continuous line is the difference for the VALC model and the dashed line is for the C07 model. The maximum difference for both model is at 20 GHz.